Spectral model for clear sky atmospheric longwave radiation

Mengying Li, Zhouyi Liao, Carlos F.M. Coimbra*

Department of Mechanical and Aerospace Engineering, Jacobs School of Engineering, Center of Excellence in Renewable Resource Integration and Center for Energy Research, University of California in San Diego, 9500 Gilman Drive, La Jolla, CA, 92093, USA

ARTICLE INFO

ABSTRACT

An efficient spectrally resolved radiative model is used to calculate surface downwelling longwave (DLW) radiation ($0 \sim 2500\,\mathrm{cm}^{-1}$) under clear sky (cloud free) conditions at the ground level. The wavenumber spectral resolution of the model is $0.01\,\mathrm{cm}^{-1}$ and the atmosphere is represented by 18 non-uniform plane-parallel layers with pressure in each layer determined on a pressure-based coordinate system. The model utilizes the most up-to-date (2016) HITRAN molecular spectral data for 7 atmospheric gases: H_2O, CO_2, O_3, CH_4, N_2O, O_2 and N_2. The MT_CKD model is used to calculate water vapor and CO_2 continuum absorption coefficients. Longwave absorption and scattering coefficients for aerosols are modeled using Mie theory. For the non-scattering atmosphere (aerosol free), the surface DLW agrees within 2.91% with mean values from the InterComparison of Radiation Codes in Climate Models (ICRCCM) program, with spectral deviations below $0.035\,\mathrm{W\,cm\,m}^{-2}$. For a scattering atmosphere with typical aerosol loading, the DLW calculated by the proposed model agrees within 3.08% relative error when compared to measured values at 7 climatologically diverse SURFRAD stations. This relative error is smaller than a calibrated parametric model regressed from data for those same 7 stations, and within the uncertainty ($+/-$ 5 W m^{-2}) of pyrgeometers commonly used for meteorological and climatological applications. The DLW increases by $1.86 \sim 6.57$ W m^{-2} when compared with aerosol-free conditions, and this increment decreases with increased water vapor content due to overlap with water vapor bands. As expected, the water vapor content at the layers closest to the surface contributes the most to the surface DLW, especially in the spectral region $0 \sim 700\,\mathrm{cm}^{-1}$. Additional water vapor content (mostly from the lowest 1 km of the atmosphere) contributes to the spectral range of $400 \sim 650\,\mathrm{cm}^{-1}$. Low altitude aerosols (~ 3.46 km or less) contribute to the surface value of DLW mostly in the spectral range $750 \sim 1400\,\mathrm{cm}^{-1}$.

1. Introduction

Absorption and scattering of shortwave solar irradiance ($< 4\,\mu$m) in the Earth's atmosphere is balanced by absorption, emission, and scattering of longwave radiation ($> 4\,\mu$m) [1]. This balance between the shortwave radiation and the longwave radiation determines the temperature structure of the atmosphere and local temperature values on Earth's surface [2]. Surface downwelling longwave irradiance (DLW) plays a critical role on weather and climate variability modeling, as well as on the heat balance design of solar power plants, of radiant cooling systems, and of the built environment [3].

Surface DLW can be measured directly by pyrgeometers, but pyrgeometers are not widely available in weather stations due to capital and calibration expenses. Furthermore, infrared radiation from the surroundings tend to complicate the installation of

research-quality pyrgeometers. Because of the importance of surface DLW on the thermal balance of both agricultural and industrial environments, simplified models to estimate the so-called sky radiosity have been proposed (see [3] for an extensive review and up-to-date data-driven models). A simple-to-use parametric model with coefficients regressed from measurements can be used to calculate the ground level longwave irradiance with satisfactory accuracy. However, for locations without pyrgeometers, choosing a parametric model with regression coefficients estimated from the measurements of other locations may introduce bias errors because the surface level downwelling irradiance depends on local meteorological conditions. This work aims to develop a *minimal* model for calculating the atmospheric downwelling longwave radiation within the uncertainty of commonly used pyrgeometers.

A spectrally resolved radiative model is developed to calculate the interactions of longwave irradiance with atmospheric molecules and aerosols. When compared with other available radiative models [4–7], this model incorporates the most up-to-date HIgh Resoluton TRANsmission (HITRAN) molecule spectral

* Corresponding author.
E-mail address: ccoimbra@ucsd.edu (C.F.M. Coimbra).

Table 1
Main components of the proposed model.

Model components	Descriptions	Presented in
Main radiative model	Divides the atmosphere into N parallel layers, constant σ system for pressures	Section 2.1
Temperature profile	AFGL profiles	Section 2.1
Concentration profiles of atmospheric gases	AFGL profiles corrected to current surface concentrations of gases	Section 2.1
Spectral resolution	Wavenumber range from 0 to 2500 cm^{-1} with resolution of 0.01 cm^{-1}	Section 2.1
Aerosol absorption and scattering coefficients	Evaluated using Mie theory	Section 2.2.1
Aerosol size distribution	Assumes equivalent spherical shape for the aerosols, size distribution follows a bimodal lognormal distribution	Section 2.2.1
Aerosol interaction with water vapor	Aerosol size and refraction index change with respect to water vapor concentration in the surrounding air	Section 2.2.1
Spectral line absorption coefficients	HITRAN 2016 absorption coefficients for 7 atmospheric gases: H_2O, CO_2, O_3, CH_4, N_2O, O_2 and N_2 evaluated at layer-averaged pressures and temperatures. Data retrived via HITRAN API	Section 2.2.2
Continuum absorption coefficients	MT_CKD water vapor and CO_2 continuum model	Section 2.2.2
Monochromatic flux of scattering medium	Scale anisotropic scattering to isotropic by δ-M approximation, use exponential integral as transfer factors, blackbody emissive power of each layer is evaluated at layer average temperature	Section 2.3.1
Broadband flux	Integrated monochromatic flux density	Section 2.3.2

line data combined with the Mlawer-Tobin-Clough-Kneizys-Davies (MT_CKD) water vapor and CO_2 continuum model [8,9]. The proposed model incorporates Mie theory to calculate aerosol extinction coefficients and asymmetry factors, with modifications for aerosol size distribution and refraction index corrections for aerosol - water vapor interactions. The complete model is a robust and inexpensive tool to study longwave radiative heat transfer in the atmosphere. The robustness of the model is derived from the use of a standard atmosphere that can be readily adjusted for surface altitude. The model was designed to be applied to the Air Force Geophysics Laboratory (AFGL) midlatitude summer atmosphere by simple displacement of the local altitude above sea level (see Section 3.3 for details).

In building the complete model, a recognition that most of the complexity related to the mutual interactions between atmosphere layers, aerosols and participating gases cannot be resolved without a detailed spectral consideration of each component. Thus, the model adopts high-resolution line-by-line data for all main constituents. The monochromatic thermal exchange between layers is calculated by an isotropic *two-stream* (or *two-flux*) model [10–13], where the piecewise monochromatic sections of the spectrum are first treated as perfect emitters before they are recursively corrected by the application of a reflective plating algorithm. This application of the plating algorithm originally proposed by Edwards [14] for radiative enclosures allows for expedited incorporation of piecewise non-black portions of the spectrum, including aerosol scattering. To the best of our knowledge, this type of recursive plating algorithm has not been applied to atmospheric radiation problems before. The combination of reusable transfer factors, high-resolution line-by-line spectral data, and the recursive plating algorithm results in a fast computational method that can be performed in real-time (within realistic time constants of change of temperature and relative humidity) by a mini computer (e.g., Raspberry Pi or BeagleBone), thus allowing for the development of smart instruments for DLW calculations as opposed to relying on sparse pyrgeometer data networks. Because the proposed model incorporates the main thermal radiation contributions in the atmosphere, it can also be used to study the sensitivity of DLW to greenhouse gases (H_2O, CO_2 and CH_4) and aerosols by adjusting the parameters in the model without the need for local telemetry.

The main components of the proposed spectral model are outlined in Table 1, and the detailed methodology used for evaluation is presented in Section 2. The model is validated in Section 3, and model results are discussed in Section 4. Main conclusions of this study are presented in Section 5.

2. The radiative model

2.1. Overview of model structure

This section presents the method used to divide the atmosphere into N parallel layers, with pressure, temperature and constituent profiles along the z direction. As depicted in Fig. 1, the atmosphere is divided in N layers, extending from the surface to an altitude with approximately zero pressure. The layers are determined according to pressure, not physical height. The monochromatic downwelling and upwelling fluxes q_n^- and q_n^+ are evaluated at layer boundaries. The monochromatic extinction coefficient κ_e, single scattering albedo $\tilde{\rho}$ and asymmetry factor g for each layer are evaluated using layer-averaged pressure $\bar{P}_n$ and temperature $\bar{T}_n$ values.

A constant σ_n coordinate system designates the average pressure $\bar{P}_n$ and the pressure of each layer boundary [15,16]:

$$\sigma_n = \frac{2N - 2n + 1}{2N},$$
$$\bar{P}_n = \sigma_n^2(3 - 2\sigma_n),$$
$$P_n = \bar{P}_{n-0.5} \tag{1}$$

and the pressure-averaged temperature of layer n is:

$$\bar{T}_n = \frac{T_n(P_n - \bar{P}_n) + T_{n+1}(\bar{P}_n - P_{n+1})}{P_n - P_{n+1}}. \tag{2}$$

AFGL profiles [17] are used for the temperature profile T_n and pressure profile P_n (Fig. 2). Since the pressure is defined by Eq. (1), the z_n and T_n are inferred from P_n according to the AFGL profiles. The AFGL midlatitude summer profile is used throughout this work, unless noted otherwise.

Seven participating atmospheric gases are considered: water vapor (H_2O), carbon dioxide (CO_2), ozone (O_3), methane (CH_4), nitrous oxide (N_2O), oxygen (O_2) and nitrogen (N_2). The vertical profiles of those gases are also based on AFGL profiles [17], with modifications to account for various surface conditions (Fig. 2). For each gas, the vertical profile of the volumetric mixing ratio is given by

$$w(z) = w^*(0) \frac{w_{\text{AFGL}}(z)}{w_{\text{AFGL}}(0)}, \tag{3}$$

where $w^*(0)$ represents the current surface volumetric mixing ratio. For H_2O, $w^*(0)$ is a function of surface relative humidity ϕ_1, such that

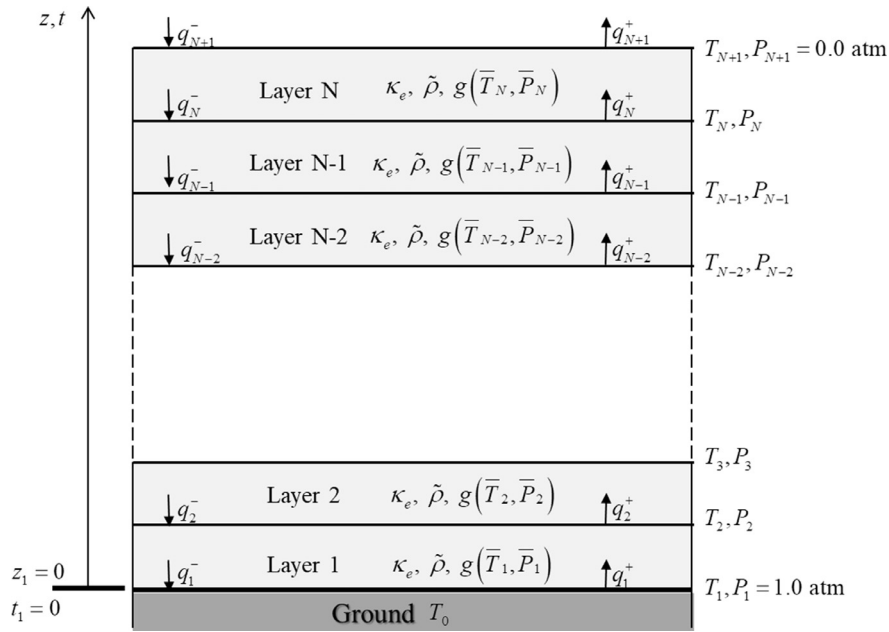$$w_{H_2O}^*(0) = \frac{\phi_1 P_s(T_1)}{P_1}. \tag{4}$$

Fig. 1. Schematic representation of the multilayer model of the Earth-atmosphere system. The vertical coordinates of altitude and normal optical path are labeled as z and t, respectively. The surface altitude z and normal optical depth t are equal to zero.
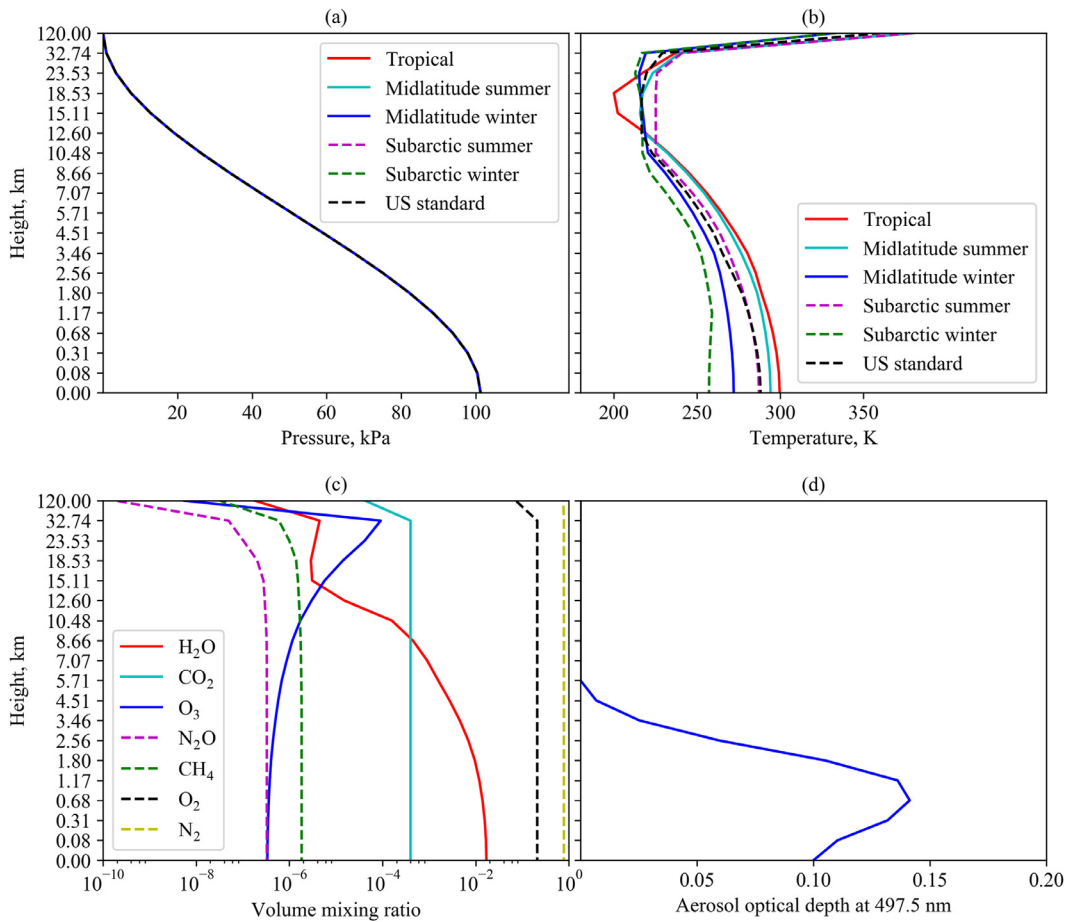

Fig. 2. (a) AFGL pressure profiles; (b) AFGL temperature profiles; (c) AFGL midlatitude summer gas profiles corrected for current surface concentration of gases (shown for 70% surface relative humidity); (d) aerosol optical depth at 497.5 nm.

The saturated water vapor pressure P_s (Pa) for a given temperature T (K) is calculated using the August-Roche-Magnus (ARM) expression [18]

$$P_s(T) = P_{ARM} \exp\left(\frac{c_{ARM}(T - 273.15)}{T - 30.11} \right), \qquad (5)$$

where $P_{ARM} = 610.94$ Pa and $c_{ARM} = 17.625$.

For the other gases we use current averaged values for the volumetric mixing ratios $w^*(0)$ in the troposphere [19]: $w^*_{CO_2}(0) = 399.5$ ppm, $w^*_{O_3}(0) = 337$ ppm, $w^*_{CH_4}(0) = 1834$ ppb, $w^*_{N_2O}(0) = 328$ ppb, $w^*_{O_2}(0) = 0.209$ and $w^*_{N_2}(0) = 0.781$.

The vertical aerosol concentration profile is adopted from [20] using the Cloud Aerosol LIDAR and Infrared Pathfinder Satellite Observations (CALIPSO) over North America. As mentioned before, we cover the wavenumber range from 0 to 2500 cm^{-1} in order to include all bands of practical interest, and adopt a spectral resolution of 0.01 cm^{-1}.

2.2. Monochromatic volumetric extinction coefficients

The atmosphere is assumed to contain seven participating gases plus aerosols. For longwave radiation, scattering by gas molecules can be neglected [1], so only scattering by aerosols is considered here. The monochromatic volumetric extinction coefficient and the single scattering albedo for each layer are expressed as (the subscript for wavenumber ν is omitted in this section for expediency),

$$\kappa_e = \kappa_a + \kappa_s = \kappa_{a,gas} + \kappa_{a,aer} + \kappa_{s,aer},$$
$$\tilde{\rho} = \frac{\kappa_{s,aer}}{\kappa_e}, \qquad (6)$$

where coefficients of gases and aerosols are evaluated at layer averaged temperature $\bar{T}_n$ and pressure $\bar{P}_n$. The absorption and scattering coefficients of aerosols follow Mie theory behavior, as detailed in the following Section 2.2.1 and Appendix A. The method we use to calculate absorption coefficients for gas mixtures is detailed in Section 2.2.2.

2.2.1. Absorption and scattering coefficients of aerosols

The monochromatic absorption coefficient $\kappa_{a,aer}$, scattering coefficient $\kappa_{s,aer}$ and asymmetry factor g_{aer} of aerosols are functions of aerosol size distribution and aerosol refractive index.

The size distribution of aerosol particles in the model follows a standard lognormal distribution [21],

$$\frac{dN}{d\ln r} = r\frac{dN}{dr} = rn(r) = \sum_{i=1}^{I} \frac{N_i}{\sqrt{2\pi}\ln\sigma_i} \exp\left[-\frac{1}{2}\left(\frac{\ln(r/r_{m,i})}{\ln\sigma_i} \right)^2 \right]. \qquad (7)$$

For each mode i, $r_{m,i}$ (μm) is the mode radii, σ_i (μm) is the standard deviation and N_i is the mode amplitude. For internally mixed aerosols (aerosols mixed as a homogeneous material that reflects the chemical and physical average of all the contributing components [22]), the size distribution can be expressed bimodally with $I = 2$ and $r_{m,1} = 0.135$ μm, $r_{m,2} = 0.995$ μm, $\sigma_1 = 2.477$ μm, $\sigma_2 = 2.051$ μm [21]. The smaller particle mode is dominant given that $N_1 = 10^4 N_2$. Since the composition and size distribution of atmospheric aerosols vary greatly with time and locations [23], aerosols modeled in [21] are used to demonstrate the proposed model. Different aerosol compositions and size distributions can be easily implemented in the model.

To account for the changes of aerosol size distribution and refractive index due to the interaction with water vapor, a growth factor g_f is used. The value of g_f is a function of surrounding relative humidity as tabulated in Table 2 [21]. The value of g_f is multiplied by the mode radii $r_{m,i}$ in Eq. (7) to account for size changes,

and is used in the following relation to account for the change of refractive index m [21]:

$$m = m_0 g_f^{-3} + m_w(1 - g_f^{-3}), \qquad (8)$$

where the subscript 0 stands for dry aerosols, and the subscript w stands for liquid water. The spectral refractive index of dry aerosols m_0 and liquid water m_w are plotted in Fig. 3. Data for these plots were obtained from Ref [21]. and [24], respectively.

The scattering of longwave radiation by aerosols is modeled by Mie theory (see Appendix A), assuming equivalent spherical shapes for the aerosols [1].

The scattering and absorption coefficients of atmospheric aerosols are proportional to N_1, the first mode amplitude, as shown in Eqs. (7) and (A5). Aerosol content in the atmosphere relates to aerosol optical depth (AOD) [25], which is defined as AOD $= \kappa_{e,aer}\bar{L}$ [26], where $\bar{L}$ is the scale height. Here we take the value of $\bar{L}$ to be 1575 m, the annualized average value reported in [20] for the continental USA. If AOD$_{497.5} = 0.1$, aerosol extinction coefficient at 497.5 nm is then $\kappa_{e,aer@497.5} = $ AOD$_{497.5}/\bar{L} = 6.35 \times 10^{-7}$ cm^{-1}. The value of N_1 in Eq. (7) is thus determined from $\kappa_{e,aer@497.5} = 6.35 \times 10^{-7}$ cm^{-1}. Fig. 4 is a plot of the monochromatic extinction coefficient and optical depth of aerosols when AOD$_{497.5} = 0.1$ and relative humidity of 70%.

2.2.2. Absorption coefficients of a mixture of atmospheric gases

The volumetric absorption coefficient κ_a (cm^{-1}) of a gas mixture is [1,27],

$$\kappa_{a,gas} = \sum_i \rho_i \kappa_i^* = \sum_i \rho_i \left[\kappa_{cont,i}^* + \kappa_{line,i}^* \right], \qquad (9)$$

where ρ_i (g cm^{-3}) is the partial density of gas i which is integrated over a layer; κ_i^* (cm^2 g^{-1}) is the mass absorption coefficient of gas i, which is the summation of continuum absorption coefficient $\kappa_{cont,i}^*$ and spectral line absorption coefficient $\kappa_{line,i}^*$.

The spectral line absorption coefficients $\kappa_{line,i}^*$ are obtained from HITRAN database using the HITRAN API [8,28]. We use a Lorentz profile with line wing cut-off set to 25 cm^{-1} as suggested by [2,9,29] to properly account for the continuum absorption for water vapor. Although the Lorentz line shape is not strictly valid for high altitudes, the contributions from higher altitudes to the surface DLW is small enough that the error in assuming Lorentz line shapes across the atmosphere is negligible (see Section 4 for more details). The methods to calculate the continuum absorption for water vapor and carbon dioxide are detailed in Appendix B.

2.3. Radiative heating/cooling fluxes

This section presents the complete method used to calculate monochromatic downwelling and upwelling fluxes at each layer boundary in a scattering atmosphere. The broadband longwave fluxes is the integration of monochromatic fluxes over the range of wavenumbers considered (0 – 2500 cm^{-1}).

2.3.1. Monochromatic fluxes

This subsection details the method used to calculate downwelling and upwelling fluxes in a scattering medium from the irradiance G_i and radiosity J_i of each atmospheric layer.

For Earth's atmosphere, the albedo for single scattering is large in some spectral regions as shown in Fig. 5, thus scattering cannot be completely neglected even though the aerosol scattering effects for longwave radiation are never dominant. For longwave radiation, the asymmetry parameter ranges from 0.02 to 0.75 as shown in Fig. 5, therefore the δ-M approximation is used to scale anisotropic scattering to isotropic before applying the following algorithm for

Table 2

Growth factor of aerosols [21]. Starred values are interpolated in the proposed model.

Relative humidity,%	0	10	20	30	40	50	60	70	80	90	100
Growth factor	1.000*	1.000*	1.000*	1.031	1.055	1.09	1.15	1.26	1.554	1.851	2.151*
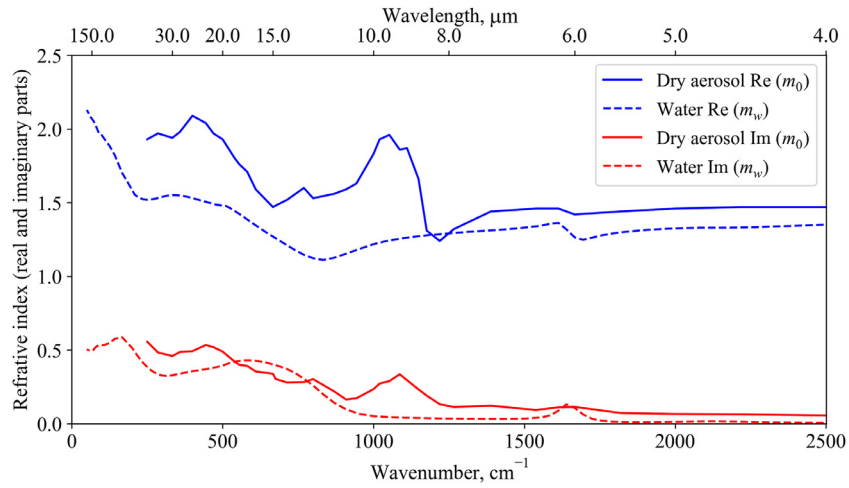
Fig. 3. Refractive index of aerosols and liquid water [21,24]. Re(·) and Im(·) stand for the real and imaginary parts of the index.
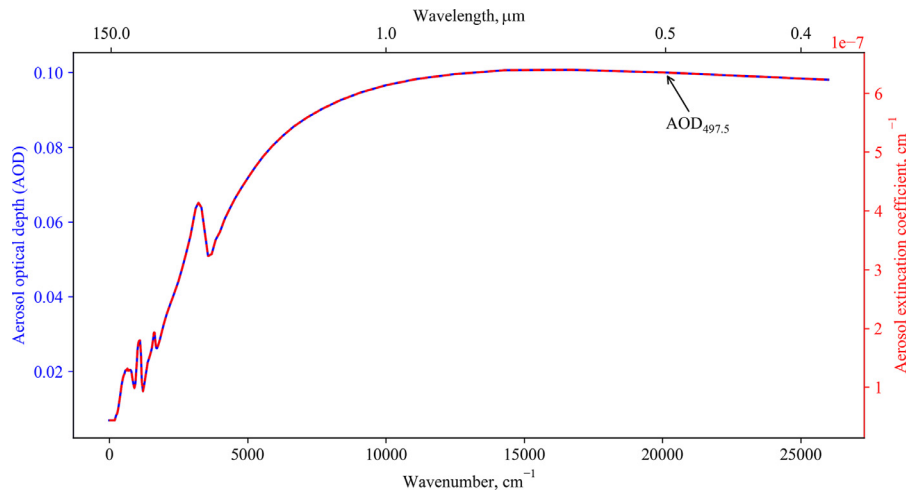
Fig. 4. The monochromatic extinction coefficient and optical depth of aerosols when $AOD_{497.5} = 0.1$ and 70% RH.
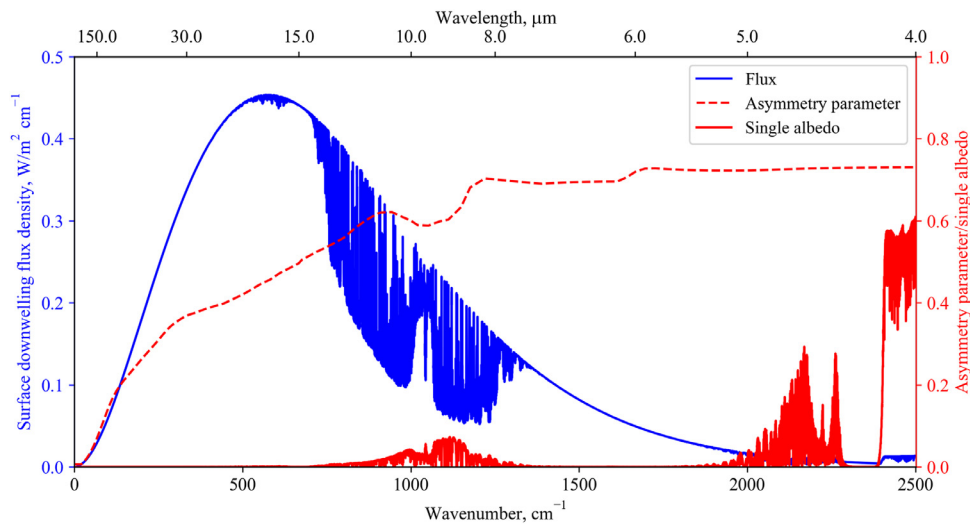
Fig. 5. The spectral surface downwelling flux density, single scattering albedo and asymmetry parameter of the nearest atmosphere layer, for surface RH = 70% and $AOD_{497.5} = 0.1$.

flux calculation. The δ-M approximation scales the extinction coefficient and the single albedo using [30],

$$\hat{\kappa}_e = (1 - \tilde{\rho}g)\kappa_e,$$

$$\hat{\tilde{\rho}} = \frac{\tilde{\rho}(1-g)}{1 - \tilde{\rho}g}. \tag{10}$$

After the scaling, isotropic scattering is assumed in the proposed model to reduce computational complexity.

For each layer n with a single albedo $\hat{\tilde{\rho}}_n$ and extinction coefficient $\hat{\kappa}_{e,n}$, the irradiance G_n and radiosity J_n are,

$$G_n = \sum_{j=0}^{N+1} \mathcal{F}_{n,j} J_j,$$

$$J_n = (1 - \hat{\tilde{\rho}}_n)\pi \bar{I}_{b,n} + \hat{\tilde{\rho}}_n G_n, \tag{11}$$

where $\mathcal{F}_{n,j}$ is the transfer factor between layer n and layer j, and $\pi \bar{I}_{b,n}$ is the averaged blackbody emissive flux of the layer, which is taken to be $\pi I_b(\bar{T}_n)$. Note that j values range from 0 to $N+1$ where layer 0 represents the ground layer and optical depth t_0 is taken to be negative infinity $(-\infty)$. Layer $N+1$ represents the outer space layer and optical depth t_{N+2} is taken to be positive infinity $(+\infty)$.

The symbol I_b (W m m^{-2} sr^{-1}) is used for the monochromatic intensity in wavenumber basis,

$$I_b(\nu, T) = \frac{2\,hc^2\nu^3}{\exp\left(\frac{hc\nu}{k_B T}\right) - 1}, \tag{12}$$

where ν (m^{-1}) is wavenumber, $h = 6.626 \times 10^{-34}$ J s is Planck's constant, $c = 3 \times 10^8$ m s^{-1} is the speed of light in vacuum and $k_B = 1.38 \times 10^{-23}$ J K^{-1} is the Boltzmann constant.

The transfer factors $\mathcal{F}_{n,j}$ are calculated as (see Appendix C for more details),

$$A_n^* \mathcal{F}_{n,j} = 2E_3\left(|t_j - t_{n+1}|\right) + 2E_3\left(|t_{j+1} - t_n|\right)$$
$$- 2E_3\left(|t_j - t_n|\right) - 2E_3\left(|t_{j+1} - t_{n+1}|\right) \quad \text{for } j \neq n,$$

$$\mathcal{F}_{n,n} = 1 - \frac{1 - 2E_3(t_{n+1} - t_n)}{2(t_{n+1} - t_n)} \quad \text{for } j = n, \tag{13}$$

where A_n^* is the equivalent surface area. For gas layers, $A_n^* = 4\hat{\kappa}_{e,n}\Delta z_n$ and for outer space and ground surface, $A_n^* = 1$. t_j is the normal optical path, $t_j = \int_0^{z_j} \hat{\kappa}_e(z')dz'$. The symbol $E_3(\cdot)$ corresponds to the third order exponential integral function with the definition of $E_3(t) = \int_1^{+\infty} \exp(-ut)/u^3 du$, which considers the diffuse radiation over all solid angles.

The irradiance G_n and radiosity J_n are then assembled in a matrix and solved by matrix reduction,

$$q_n^+ = \sum_{j=0}^{n-1} \mathcal{F}_{n,j}^* J_j, \tag{14}$$

where $\mathcal{F}_{n,j}^*$ represent corrected transfer factors for downward and upward fluxes calculation. The values of $\mathcal{F}_{n,j}^*$ are calculated using Eq. (13) with the following rules for optical depth re-determination: (1) when calculating downward fluxes q_n^-, t_0 to t_{n-1} are taken to be $-\infty$; (2) when calculating upward fluxes q_n^+, t_{n+1} to t_{N+2} are taken to be $+\infty$.

Note that the above matrix reductions are calculated on every wavenumber, i.e. 0.25 million times with the resolution of 0.01 cm^{-1} for spectral range from 0 cm^{-1} to 2500 cm^{-1}. To make the model more computationally efficient, the irradiance G_n is solved directly by defining a modified transfer factor $\mathcal{F}_{n,j}^{**}$,

$$G_n = \sum_{j=0}^{N+1} \mathcal{F}_{n,j}^{**} \bar{I}_{b,j}, \tag{15}$$

where the modified transfer factor $\mathcal{F}_{n,j}^{**}$ is calculated from the blackbody transfer factors $\mathcal{F}_{n,j}$ (Eq. (13)) recursively using a modified plating algorithm first proposed by Edwards [14] for radiative transfer within enclosures, but here adapted to radiative exchange between atmospheric layers with scattering,

$$\begin{cases} \mathcal{F}_{i,j}^{**} = \mathcal{F}_{i,j} + \frac{\hat{\tilde{\rho}}_k}{D_k} \mathcal{F}_{i,k} \mathcal{F}_{k,j}, & i \neq k, j \neq k, \\ \mathcal{F}_{i,k}^{**} = \frac{1 - \hat{\tilde{\rho}}_k}{D_k} \mathcal{F}_{i,k}, & i \neq k, j = k, \\ \mathcal{F}_{k,j}^{**} = (1 - \hat{\tilde{\rho}}_k)\left[\mathcal{F}_{k,j} + \frac{\hat{\tilde{\rho}}_k}{D_k} \mathcal{F}_{k,k} \mathcal{F}_{k,j}\right] = \frac{\hat{\tilde{\rho}}_k}{D_k} \mathcal{F}_{k,j}, & i = k, j \neq k, \\ \mathcal{F}_{k,k}^{**} = \frac{(1 - \hat{\tilde{\rho}}_k)^2}{D_k} \mathcal{F}_{k,k}, & i = k, j = k. \end{cases} \tag{16}$$

where $D_k = 1 - \hat{\tilde{\rho}}_k \mathcal{F}_{k,k}$.

The wavenumbers are vectorized when calculating the modified transfer factors, so the computational performance is improved in comparison to matrix reductions. More details about the computational performance of the overall algorithm are given in Section 4.4.

2.3.2. Broadband fluxes

The broadband flux is the integration of monochromatic flux over the considered longwave wavenumber range,

$$\mathbf{q}_n^- = \int_{\nu_1}^{\nu_2} q_n^-(\nu)d\nu,$$

$$\mathbf{q}_n^+ = \int_{\nu_1}^{\nu_2} q_n^+(\nu)d\nu, \tag{17}$$

$$\begin{pmatrix} G_0 \\ G_1 \\ \vdots \\ G_N \\ G_{N+1} \\ J_0 \\ J_1 \\ \vdots \\ J_N \\ J_{N+1} \end{pmatrix} = \begin{pmatrix} 0 & 0 & \cdots & 0 & 0 & \mathcal{F}_{0,0} & \mathcal{F}_{0,1} & \cdots & \mathcal{F}_{0,N} & \mathcal{F}_{0,N+1} \\ 0 & 0 & \cdots & 0 & 0 & \mathcal{F}_{1,0} & \mathcal{F}_{1,1} & \cdots & \mathcal{F}_{1,N} & \mathcal{F}_{1,N+1} \\ \vdots & \vdots & \vdots & \vdots & \vdots & \vdots & \vdots & \vdots & \vdots & \vdots \\ 0 & 0 & \cdots & 0 & 0 & \mathcal{F}_{N,0} & \mathcal{F}_{N,1} & \cdots & \mathcal{F}_{N,N} & \mathcal{F}_{N,N+1} \\ 0 & 0 & \cdots & 0 & 0 & \mathcal{F}_{N+1,0} & \mathcal{F}_{N+1,1} & \cdots & \mathcal{F}_{N+1,N} & \mathcal{F}_{N+1,N+1} \\ \hat{\tilde{\rho}}_0 & 0 & \cdots & 0 & 0 & 0 & 0 & \cdots & 0 & 0 \\ 0 & \hat{\tilde{\rho}}_1 & \cdots & 0 & 0 & 0 & 0 & \cdots & 0 & 0 \\ \vdots & \vdots & \ddots & \vdots & \vdots & \vdots & \vdots & \vdots & \vdots & \vdots \\ 0 & 0 & \cdots & \hat{\tilde{\rho}}_N & 0 & 0 & 0 & \cdots & 0 & 0 \\ 0 & 0 & \cdots & 0 & \hat{\tilde{\rho}}_{N+1} & 0 & 0 & \cdots & 0 & 0 \end{pmatrix} \begin{pmatrix} G_0 \\ G_1 \\ \vdots \\ G_N \\ G_{N+1} \\ J_0 \\ J_1 \\ \vdots \\ J_N \\ J_{N+1} \end{pmatrix} + \begin{pmatrix} 0 \\ 0 \\ \vdots \\ 0 \\ 0 \\ (1 - \hat{\tilde{\rho}}_0)\pi \bar{I}_{b,0} \\ (1 - \hat{\tilde{\rho}}_1)\pi \bar{I}_{b,1} \\ \vdots \\ (1 - \hat{\tilde{\rho}}_N)\pi \bar{I}_{b,N} \\ (1 - \hat{\tilde{\rho}}_{N+1})\pi \bar{I}_{b,N+1} \end{pmatrix}.$$

With the values of J_j determined, the downward and upward fluxes are calculated as,

$$q_n^- = \sum_{j=n}^{N+1} \mathcal{F}_{n,j}^* J_j,$$

where $q_n^-(\nu)$ / $q_n^+(\nu)$ is monochromatic downward / upward flux and ν (cm^{-1}) is wavenumber in the range of $\nu_1 = 0$ cm^{-1} and $\nu_2 = 2500$ cm^{-1}. Broadband integration is evaluated using a trapezoidal rule.
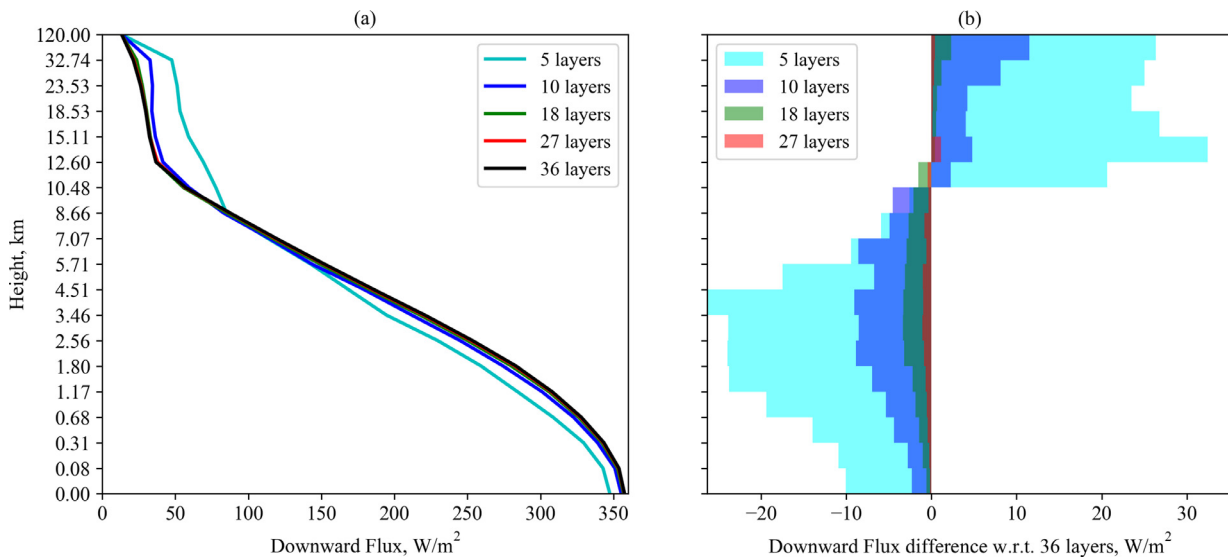
Fig. 6. (a) Grid dependence on number of layers for broadband DLW; (b) Broadband DLW difference when compared to 36 layers. For this numerical example, surface relative humidity is 70% and $AOD_{497.5}$ is 0.1. The downwelling flux at the top of the atmosphere is from solar radiation.

Table 3
Comparison of surface DLW with ICRCCM results. A midlatitude summer profile is used and the flux values have unit of W m^{-2}.

Case	Case description	ICRCCM Mean [31]	ICRCCM Std [31]	Reference [32]	This work
19	H_2O only, with continuum	326.23	14.06	333.92	335.74
20	H_2O only, without continuum	273.19	17.82	269.02	271.86
27	CO_2, H_2O, O_3 with 300 ppmv CO_2	343.18	8.21	346.91	346.78

3. Validation of the model

3.1. Grid convergence

The plane parallel model of the atmosphere assumes each layer to be homogeneous, so the accuracy of the model may be compromised if too few layers are considered. Increasing the number of layers increases model accuracy, but there is a number of layers after which further increase causes negligible effects on the overall results. As shown in Fig. 6 below, the downward flux profile changes by less than 3 W m^{-2} when 18 or more atmospheric layers are used, indicating that grid convergence for DLW is achieved.

3.2. Comparison with ICRCCM results

In this subsection we validate the proposed model against longwave results from the Intercomparison of Radiation Codes in Climate Models program (ICRCCM) [31]. Aerosols and solar longwave radiation are not included in ICRCCM results. The comparisons for selected cases are listed in Table 3, showing that the results of the proposed model are within 2.91% of the mean and within one standard deviation of ICRCCM results. The reference in Table 3 is the ICRCCM longwave results produced by Atmospheric Environmental Research, Inc. (AER), with data downloaded from [32]. The DLW flux profiles are plotted in Fig. 7 (a) where the difference compared to AER ICRCCM results is smaller than $\pm$ 8.5 W/m^2 as shown in Fig. 7 (b). Spectral comparison with results from AER ICRCCM results is plotted in Fig. 7 (c). The absolute difference is smaller than 0.035 W cm m^{-2} for all wavenumbers.

3.3. Comparison with SURFRAD measurements

The comparisons in the previous section indicate the spectral model performs well for non-scattering atmospheres. In this sec-

tion, we validate the spectral model for scattering atmosphere through a comparison with surface measurements of DLW from 7 SURFRAD stations for the year 2013. Aerosol content is assumed to be $AOD_{497.5} = 0.1243$ at the surface (the value 0.1243 is the 2013 annually averaged $AOD_{497.5}$ for all 7 stations, measured from the surface). Model results are also compared to a calibrated empirical model [3]. During clear sky daytime periods, the surface DLW can be empirically expressed as a function of surface water vapor partial pressure (in hPa),

$$\frac{DLW}{\sigma T_a^4} = \varepsilon_{sky} = c_1 + c_2\sqrt{P_w} = 0.598 + 0.057\sqrt{P_w}, \tag{18}$$

where ε_{sky} is the sky emissivity, $\sigma = 5.67 \times 10^{-8}$ W m^{-2} K^{-4} is the Stefan Boltzmann constant and T_a (K) is surface air temperature. The coefficients c_1 and c_2 are obtained by regression from data from all 7 SURFRAD stations [3].

The proposed spectral model is then used to calculate surface DLW for each of the SURFRAD stations. The SURFRAD stations are located at different altitudes, and the effect of altitude differences is modeled by placing their ground surfaces in different layers according to their altitudes, as shown in Fig. 8. The model assumes the AFGL midlatitude summer profile, while the ground level relative humidity ranges from 5% to 100% in the increment of 5%, resulting in 20 different water vapor profiles. Thus, at each altitude z, there are 20 data points of water vapor partial pressure P_w and 20 data points of sky emissivity ε_{sky}. A one-degree spline is used to interpolate the 20 data points, i.e. $\varepsilon_{sky} = spl(P_w)$ as shown in Fig. 9. At each station, the sky emissivity is calculated for different values of surface water vapor pressure using the spline interpolation. The surface DLW is then calculated from the sky emissivity using Eq. (18).

Model results are compared to measurements using three distinct error metrics: the mean biased error (MBE), the root mean
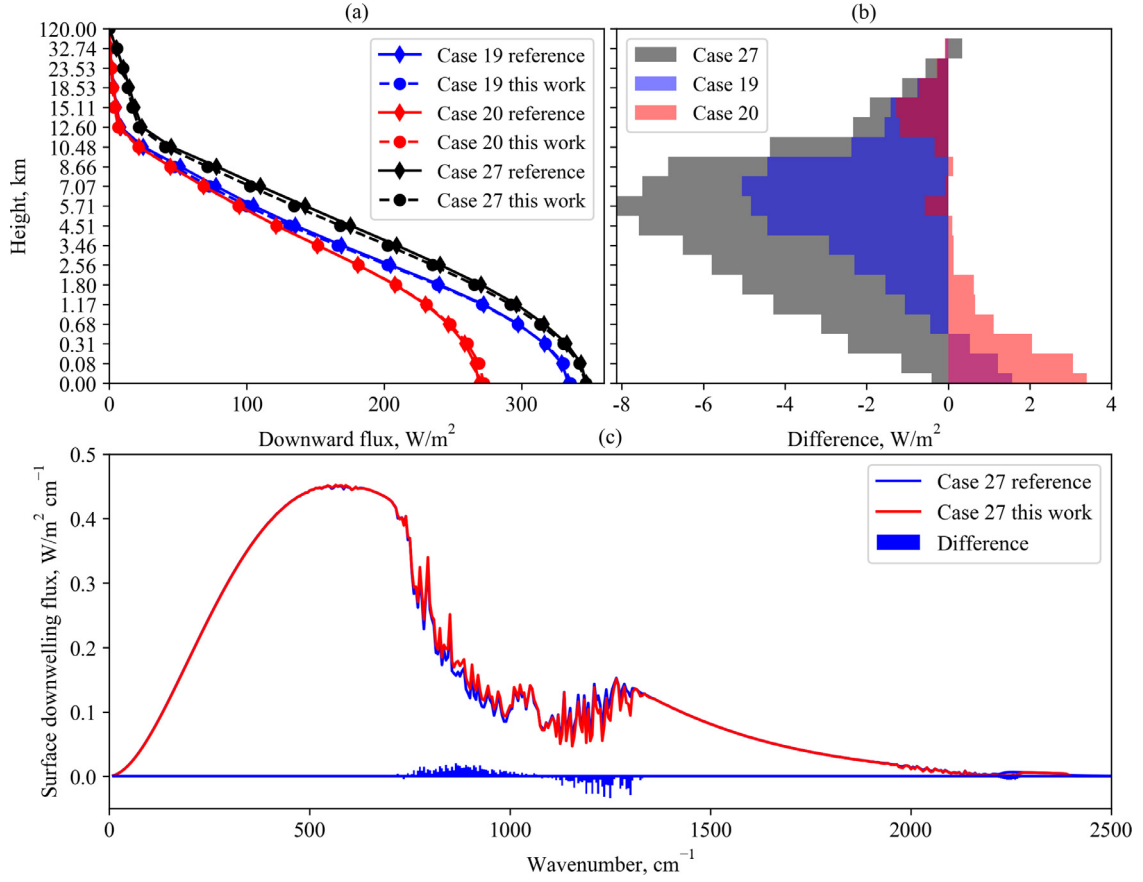
Fig. 7. (a) Comparison of DLW profiles between the proposed model and Ref [32]. (b) The difference of DLW fluxes with respect to Ref [32]. (c) Spectral comparison of surface DLW flux densities.
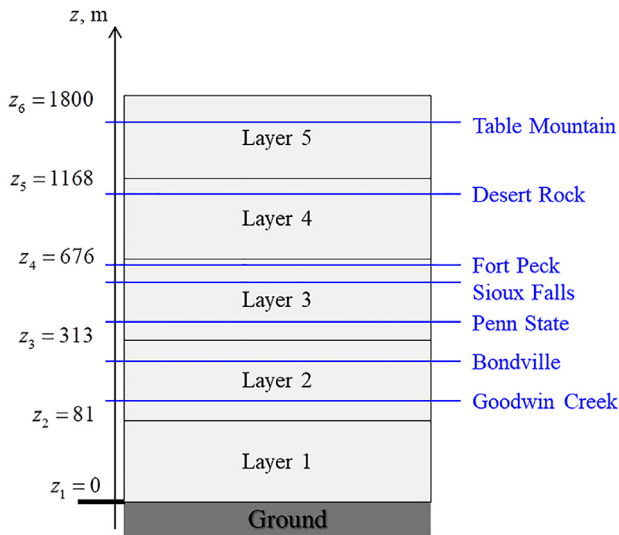

Fig. 8. Illustration of ground surface locations of the 7 SURFRAD stations used in the model application.

square error (RMSE), and the relative root mean square error (rRMSE):

$$MBE = \frac{1}{K} \sum_{k=1}^{K} \left(LW_{M,k} - LW_{S,k} \right), \tag{19}$$

$$RMSE = \sqrt{\frac{1}{K} \sum_{k=1}^{K} \left(LW_{M,k} - LW_{S,k} \right)^2}, \tag{20}$$

$$rRMSE = \frac{RMSE}{1/K \sum_{k=1}^{K} LW_{S,k}}, \tag{21}$$

where K is the number of data points in the dataset, and LW_M and LW_S are the measured and modeled longwave irradiances, respectively.

Table 4 presents the MBE, RMSE and rRMSE of the empirical model and the spectral model when compared to measurements for each individual stations. Compared to the empirical model Eq. (18), which is regressed using aggregated data from all 7 stations, the proposed spectral model yields lower RMSE (rRMSE) for 6 out of 7 stations, indicating that the spectral model is able to capture the variability between stations. The model rRMSE ranges from 2.08% to 3.08% for all stations. The performance of the model is further illustrated in Fig. 9, where biases of the empirical model are more efficiently captured by the spectral model. Note that the proposed model can also be fine-tuned to different pressure-temperature profiles of the atmosphere, but these comparisons show that the model is robust enough to perform well for different microclimates using the standard AFGL midlatitude summer profile.

4. Results and discussion

4.1. Broadband contributions of water vapor and aerosol

Broadband surface DLW as a function of surface water vapor partial pressure and $AOD_{497.5}$ is plotted in Fig. 10. The DLW increases with surface water vapor pressure as well as $AOD_{497.5}$, indicating that water vapor and aerosols are warming the surface. The aerosol warming effect is more obvious when there is little
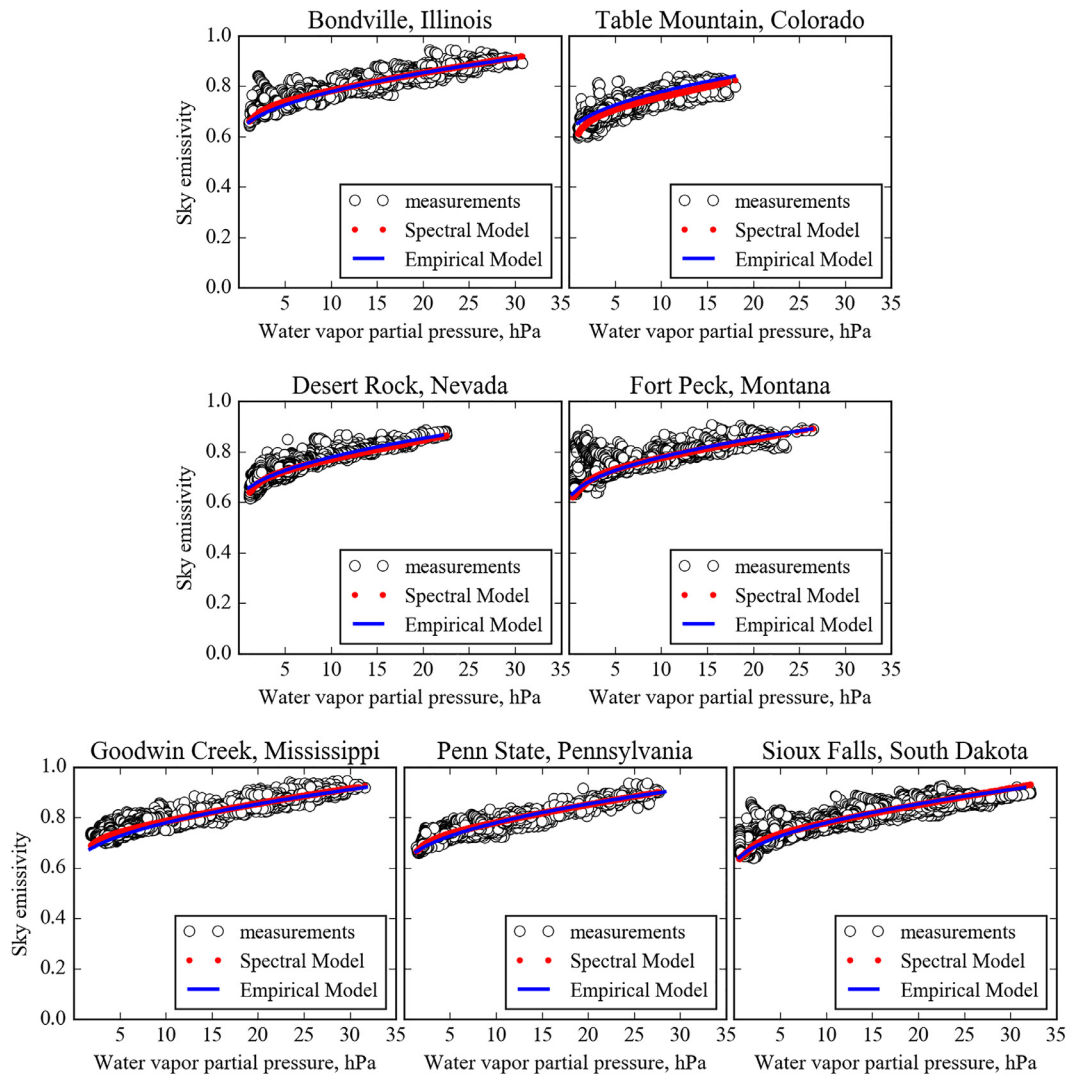
Fig. 9. Comparison of measured, empirically modeled, and spectrally modeled sky emissivities for the 7 SURFRAD stations.

Table 4
Error metrics for empirical and spectral models for estimation of surface DLW during daytime. Bold values indicate best results.

Parameters	SURFRAD Stations						
	Bondville	Table Mountain	Desert Rock	Fort Peck	Goodwin Creek	Penn State	Sioux Falls
Latitude (°)	40.05	40.13	36.62	48.31	34.25	40.72	43.73
Longitude (°)	−88.37	−105.24	−116.02	−105.10	−89.87	−77.93	−96.62
Altitude (m)	213	1689	1007	634	98	376	437
Average T_a (°C)	14.0	14.1	21.9	11.4	18.2	14.6	11.6
25th percentile of T_a (°C)	5.0	7.3	14.6	0.4	11.1	9.4	0.2
75th percentile of T_a (°C)	23.3	21.6	30.1	22.9	26.1	21.1	23.0
Average P_w (hPa)	11.9	7.2	5.1	8.9	14.3	11.1	11.1
25th percentile of P_w (hPa)	5.0	3.4	3.1	4.0	6.4	4.9	4.4
75th percentile of P_w (hPa)	18.0	10.6	5.8	13.7	21.7	16.5	17.0
Empirical MBE (W/m²)	2.64	−6.82	**3.34**	3.91	4.62	**0.46**	1.30
Empirical RMSE (W/m²)	7.62	9.70	**6.93**	9.60	8.53	7.34	9.07
Empirical rRMSE (%)	2.47	3.41	**2.18**	3.20	2.54	2.44	2.99
Computed MBE (W/m²)	**−0.02**	0.61	4.52	**3.85**	1.35	-1.58	**0.15**
Computed RMSE (W/m²)	**6.86**	**6.93**	7.65	**9.25**	6.97	**6.95**	8.68
Computed rRMSE (%)	**2.22**	**2.43**	2.40	**3.08**	2.08	**2.31**	2.86

water vapor present, which is consistent with previous works [26]. When $AOD_{497.5} = 0.1$, the aerosol direct forcing is 6.57 W m^{-2} for drier conditions (RH = 5%), and 1.86 W m^{-2} for wetter conditions (RH = 95%).

4.2. Spectral and spatial contributions of water vapor

The surface value of DLW is a result of contributions of every atmospheric layer above the surface. To examine the spectral and spatial contributions of water vapor, the modified transfer factors
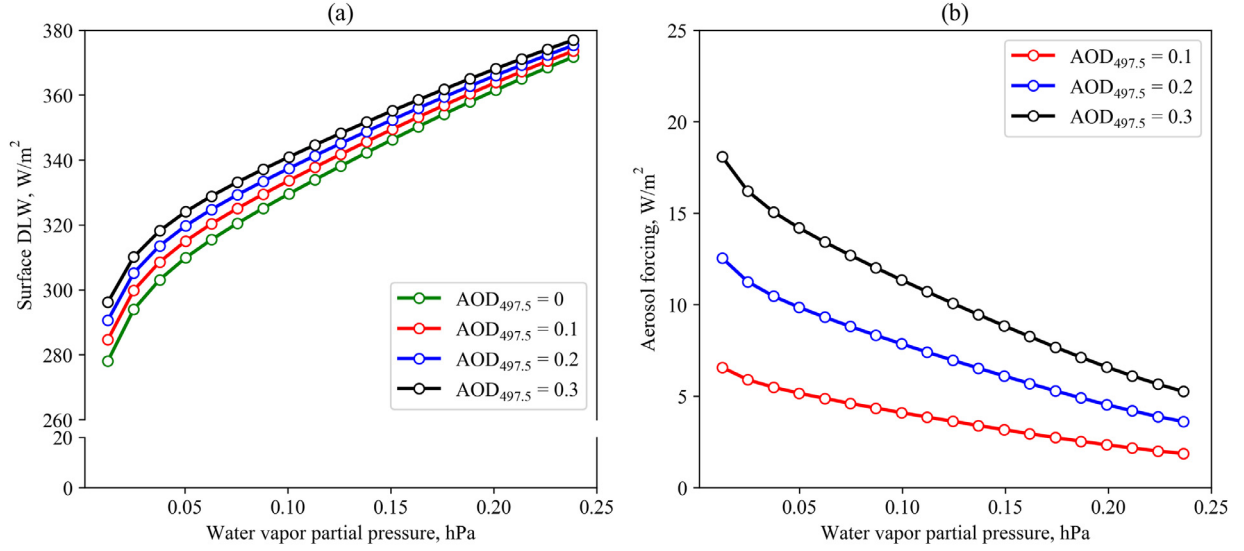
Fig. 10. Surface DLW with respect to surface water vapor partial pressure and aerosol optical depth.

$\mathcal{F}_{0,j}^{**}$ are used to express surface monochromatic DLW as,

$$q_1^- = G_0 = \sum_{j=0}^{N+1} \mathcal{F}_{0,j}^{**} \bar{I}_{b,j}. \qquad (22)$$

Fig. 11 shows the spatial and spectral contribution of water vapor to surface DLW. The left column and right column show the modified transfer factor $\mathcal{F}_{0,j}^{**}$ and monochromatic flux density $\mathcal{F}_{0,j}^{**} \bar{I}_{b,j}$ of each atmosphere layer, respectively. As shown in Fig. 11 (a1), the transfer factors for the absorbing bands of $0 \sim 400\,\mathrm{cm}^{-1}$ (H_2O), $650 \sim 750\,\mathrm{cm}^{-1}$ (CO_2), $1400 \sim 1700\,\mathrm{cm}^{-1}$ (H_2O) and $2300 \sim 2400\,\mathrm{cm}^{-1}$ (CO_2) are nearly unity in the nearest atmospheric layer, indicating the contribution to surface DLW in these bands are mostly coming from this layer (Fig. 11 (a2)). Comparing Fig. 11 (a1) and (a2), the latter two bands show relatively small contributions in (a2) than in (a1) because $\bar{I}_b$ is relatively small in these two bands. Further increasing the water vapor content has negligible effect on the surface DLW in those bands, as shown in Fig. 11 (b), (c) and (d). The contributions of water vapor is mostly from the atmosphere below 1 km in the spectral range of $400 \sim 650\,\mathrm{cm}^{-1}$. Contributions also come from the bands $750 \sim 1400\,\mathrm{cm}^{-1}$ and $1700 \sim 2300\,\mathrm{cm}^{-1}$, for heights below 3.46 km. The blue region indicates a decrease in contribution, because water vapor in the layer(s) below absorbs the emitted radiation, preventing the radiation coming from above from reaching the surface.
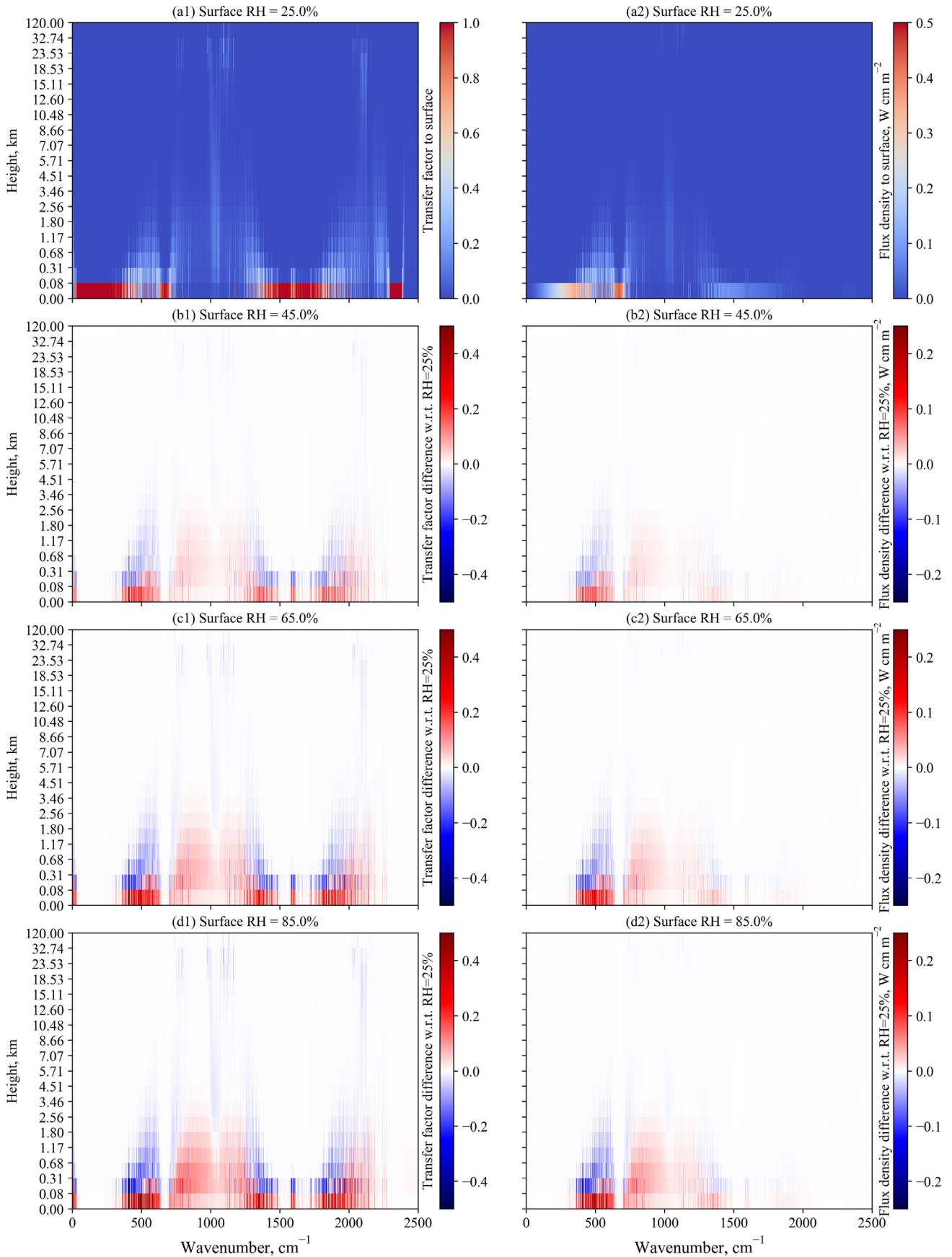
4.3. Spectral and spatial contributions of aerosols

Fig. 12 shows the spatial and spectral contributions of aerosols from each atmosphere layer, for different surface relative humidity values. The difference of transfer factor (left column) and monochromatic flux density (right column) are with respect to aerosol - free cases. The aerosol contribution to transfer factor is mostly felt within the spectral atmospheric windows: $400 \sim 650\,\mathrm{cm}^{-1}$, $750 \sim 1400\,\mathrm{cm}^{-1}$, $1700 \sim 2300\,\mathrm{cm}^{-1}$ and $2400 \sim 2500\,\mathrm{cm}^{-1}$ where the single scattering albedo is non-trivial (Fig. 5). The latter two windows have negligible effect on the monochromatic flux density because the blackbody intensities in these bands are low. Aerosol forcing mostly comes from the layers below 3.46 km. Above 3.46 km, the blue regions indicate a decrease in transfer factor and monochromatic flux density, because aerosols below prevent the emitted longwave radiation from reaching the surface. In addition, the aerosol forcing effects are accentuated when less water vapor is present, as evidenced by broadband analyses and experiments [33].

4.4. Computational performance

The algorithm proposed here employs the two-flux approximation (i.e., avoids directional discretization), reusable transfer factors and a recursive plating algorithm for aerosol scattering with the objective of improving overall computational performance for calculation of atmospheric DLW radiation using high-resolution spectral data. The complete model is easily coded in Python within a few hundred lines of code. Wavenumbers are vectorized so that CPU time is only weakly dependent on spectral resolution when adapting the plating algorithm. As a comparison with a radiation model that can also be easily coded in Python, the speed of computation of a standard Monte Carlo simulation is linearly proportional to spectral resolution. A single run of the complete model described in this work requires 100s of Intel Xeon E5-2640 CPU time, where each run corresponds to one data point in Fig. 10. The use of the recursive plating algorithm alone reduces the total computational time by 30% when compared to direct matrix reduction. By contrast, an efficient Monte Carlo simulation for the same single case using 50,000 representative photon bundles emitted from each layer requires 90 minutes in the same CPU with 100 times smaller spectral resolution ($1\,\mathrm{cm}^{-1}$). In other words, the proposed model is 3000 to 5400 times faster than an equivalent Monte Carlo simulation. Although other radiative models (e.g., those based on discrete-ordinate methods) used in commercial codes also far outperform Monte Carlo simulations in terms of CPU time consumption, there are fewer options for doing so while retaining the level of accuracy and model robustness presented here, and not requiring either thousands of lines of FORTRAN/C coding, and/or expensive yearly fees for the use of optimized commercial products. The model proposed in this work is readily and efficiently implementable in high-level, open-source interpreted computer languages like Python, can easily accommodate different pressure-temperature and aerosol profiles, is only weakly dependent on spectral resolution, and is fast enough to be computed in real-time (within time constants of interest to DLW variability) using low-cost mini-computers.

Fig. 11. Spatial and spectral contributions of water vapor to surface DLW. All differences are compared to RH = 25.0% case.
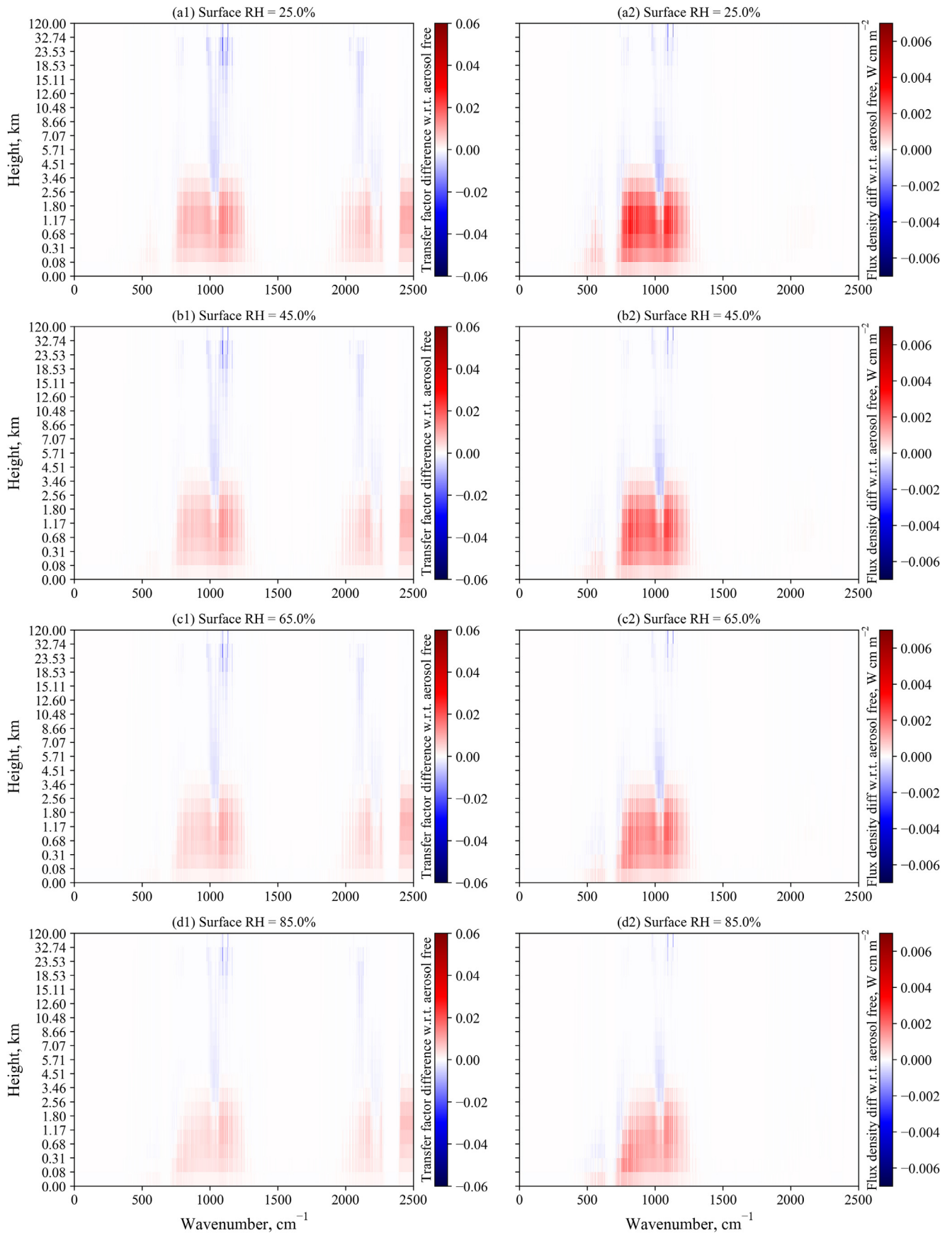
Fig. 12. Spatial and spectral contributions of aerosols to surface DLW. All differences are compared to aerosol free cases.

5. Conclusions

The primary goal of this work is to develop an effective *minimal* model that incorporates the main physical mechanisms needed for calculation of the atmospheric downwelling longwave radiation at the ground level for widely different geographical sites. The operative word *effective* here means a complete model that is capable of discerning the effects of the main contributors to DLW while allowing for fast computations that can be performed by mini computers within time frames compatible with both the time scale of variations in the atmosphere, but also with time scales of engineering systems (power plants, etc.). All main features of the model and its implementation are described within the body of this work (including the appendices).

A secondary goal of this study is to examine the effects of water vapor and aerosol content on the surface DLW at high spectral resolutions. A spectrally resolved, multi-layer radiative model is developed to calculate surface downwelling longwave (DLW) irradiance ($0 \sim 2500\,cm^{-1}$) under clear-sky (cloud-free) conditions. The wavenumber spectral resolution of the model is $0.01\,cm^{-1}$ and the atmosphere is represented by 18 non-uniform plane-parallel layers with the pressure of each layer determined by a constant σ coordinate system. Standard AFGL profiles for temperature and atmospheric gas concentrations have been adopted with the correction for current surface atmospheric gas concentrations. The model incorporates the most up-to-date (2016) HITRAN molecular spectral data for 7 atmospheric gases: H_2O, CO_2, O_3, CH_4, N_2O, O_2 and N_2. The MT_CKD model is used to calculate water vapor and CO_2 continuum absorption coefficients.

For a scattering atmosphere (with aerosols), the aerosol size distribution is assumed to follow a bimodal distribution. The size and refractive index of aerosols change as they absorb water, therefore the size distribution and refractive index are corrected for different values of local water vapor concentrations (relative humidity values). The absorption coefficients, scattering coefficients and asymmetry factors for aerosols are calculated from the refractive indices for different size distributions by Mie theory. The radiosity and irradiance of each layer are calculated by energy balance equations using transfer factors with the assumption of isotropic aerosol scattering (the δ-M approximation is used to scale anisotropic scattering). The monochromatic downwelling and upwelling fluxes with scattering for each layer are further calculated using a recursive plating algorithm. Broadband fluxes are integrated over the spectrum for both non-scattering and scattering atmospheres.

A model with 18 vertical layers is found to achieve grid independence for DLW. For a non-scattering atmosphere (aerosol free), the calculated surface DLW irradiance agrees within 2.91% with the mean values from InterComparison of Radiation Codes in Climate Models (ICRCCM) program, and the spectral density difference is smaller than $0.035\,W\,cm\,m^{-2}$. For a scattering atmosphere, the modeled DLW irradiance agrees within 3.08% relative error when compared to measured values from 7 climatologically diverse SURFRAD stations. This relative error is smaller than the error from a calibrated empirical model regressed from aggregate data for those same 7 stations, i.e., the proposed model captures the climatological differences between stations. We also note that these deviation values are within the uncertainty range (+/- 5 W m^{-2}) of pyrgeometers ($\sim$ 3% uncertainty).

When aerosol optical depth (AOD) values around 0.1 (497.5 nm/ground level) are considered, longwave aerosol forcing falls between $1.86\,W\,m^{-2}$ to $6.57\,W\,m^{-2}$. The forcing increases with decreasing values of surface water vapor content because the aerosol bands contribute mostly when the water vapor bands are not saturated. When examining the spatial and spectral contributions of water vapor to the surface DLW, we find, as expected, that water vapor in the nearest surface layer contributes the most, especially in the spectral ranges $0 \sim 400\,cm^{-1}$ and $650 \sim 700\,cm^{-1}$. Within the atmospheric spectral windows $400 \sim 650\,cm^{-1}$, $750 \sim 1400\,cm^{-1}$, $1700 \sim 2300\,cm^{-1}$ and $2400 \sim 2500\,cm^{-1}$, water vapor above 3.46 km has negligible effect on the monochromatic surface DLW. In some spectral regions, there is a decrease in water vapor forcing because water vapor content in the layers below prevents the longwave radiation from reaching the surface. The warming caused by aerosols mostly comes from the layers below 3.46 km. In a narrow spectral band between 1050 to $1150\,cm^{-1}$ above 3.46 km, there is a decrease in monochromatic surface DLW forcing, since the lower layer aerosols prevent the radiation from reaching the surface by absorption.

In summary, the proposed model is capable of capturing climatological and meteorological differences between locations when compared to extensive surface telemetry, which justifies its use for calculating DLW at other locations across the contiguous United States where measurements are not readily available. The proposed model also serves as a powerful and robust tool to study high spectral resolution interactions between atmospheric constituents within the critical longwave region of the electromagnetic spectrum.

Appendix A. Mie theory equations

The extinction, scattering, absorption efficiencies and asymmetry parameter of a single aerosol particle are calculated using standard Mie theory relations [1,34],

$$Q_{ext} = \frac{2}{x^2} \sum_{n=1}^{\infty} (2n+1)\text{Re}(a_n + b_n),$$

$$Q_{sca} = \frac{2}{x^2} \sum_{n=1}^{\infty} (2n+1)\left(|a_n|^2 + |b_n|^2\right),$$

$$Q_{abs} = Q_{ext} - Q_{sca},$$

$$g = \frac{4}{x^2 Q_{sca}} \left[\sum_{n=1}^{\infty} \frac{n(n+2)}{n+1} \text{Re}\left(a_n a_{n+1}^* + b_n b_{n+1}^*\right) \right.$$
$$\left. + \sum_{n=1}^{\infty} \frac{2n+1}{n(n+1)} \text{Re}(a_n b_n^*) \right], \tag{A1}$$

where the diacritic $*$ stands for the complex conjugate; $\text{Re}(\cdot)$ stands for the real part of a complex number; x is the size parameter, $x = 2\pi \nu r$, where r (cm) is the radius of the aerosol and ν (cm^{-1}) is the wavenumber; a_n and b_n are the Mie coefficients, which are a function of the size parameter x and the aerosol refractive index m.

Note that the above parameters are summations of infinite series, which are truncated after $n_{\max}$ terms in the computations to satisfy accuracy requirements. The criteria for the number of terms used is given by [34],

$$n_{max} = \text{round}(x + 4x^{1/3} + 2). \tag{A2}$$

When the magnetic permeability of the sphere is equal to the magnetic permeability of the ambient medium, the Mie

coefficients a_n and b_n are given by [34],

$$a_n = \frac{m^2 j_n(mx)[xj_n(x)]' - j_n(x)[mxj_n(mx)]'}{m^2 j_n(mx)[xh_n(x)]' - h_n(x)[mxj_n(mx)]'},$$

$$b_n = \frac{j_n(mx)[xj_n(x)]' - j_n(x)[mxj_n(mx)]'}{j_n(mx)[xh_n(x)]' - h_n(x)[mxj_n(mx)]'}, \quad \text{(A3)}$$

where m is the refractive index of the aerosol relative to the ambient air; $j_n(z)$ is the spherical Bessel function of the first kind; $h_n(z)$ is the spherical Bessel related function, $h_n(z) = j_n(z) + y_n(z)i$ and $y_n(z)$ is the spherical Bessel function of the second kind.

The primes indicate derivatives with respect to the arguments, $z = x$ or $z = mx$, with the derivatives of the spherical Bessel functions being [35],

$$[zj_n(z)]' = zj_{n-1}(z) - nj_n(z),$$
$$[zh_n(z)]' = zh_{n-1}(z) - nh_n(z). \quad \text{(A4)}$$

For atmospheric aerosols with varying sizes, the volumetric absorption and scattering coefficients and asymmetry parameters correspond to integrated values of scattering/absorption efficiencies over all possible aerosol radii r [1],

$$\kappa_{a,aer} = \int_0^\infty n(r)Q_{abs}(r)\pi r^2 dr,$$

$$\kappa_{s,aer} = \int_0^\infty n(r)Q_{sca}(r)\pi r^2 dr,$$

$$g_{aer} = \frac{1}{\kappa_{s,aer}} \int_0^\infty n(r)Q_{sca}(r)\pi r^2 g(r)dr. \quad \text{(A5)}$$
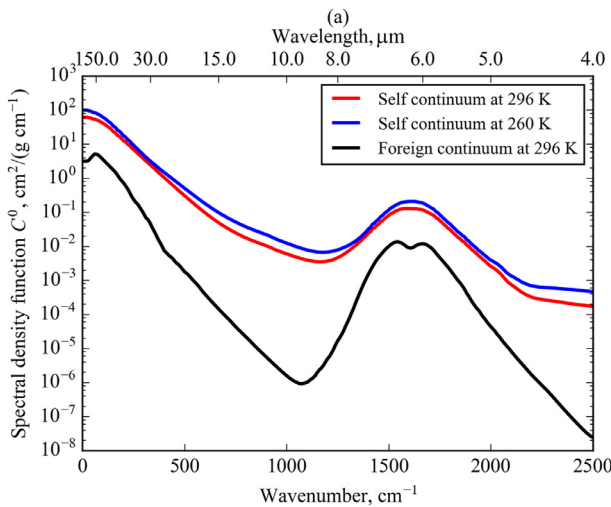
Appendix B. Continuum absorption

The continuum absorption coefficient of water vapor is the summation of self continuum and foreign continuum coefficients,

$$\kappa^*_{cont,H_2O} = \kappa^*_{self,H_2O} + \kappa^*_{frgn,H_2O}. \quad \text{(B1)}$$

The continuum absorption spectral density functions C^0 at reference conditions are obtained from the MT_CKD model [9] and plotted in Fig. B1 (a). For conditions with temperature T and pressure P, the spectral density function is,

$$C(T,P) = C_{self}(T,P) + C_{frgn}(T,P)$$

$$= \frac{P}{P_0}\frac{T_0}{T}\left[w_{H_2O}C^0_{T_0,self}\left(\frac{C^0_{T_{ref},self}}{C^0_{T_0,self}}\right)^{\frac{T-T_0}{T_{ref}-T_0}} + (1-w_{H_2O})C^0_{T_0,frgn}\right], \quad \text{(B2)}$$

where $T_0 = 296$ K, $P_0 = 1$ atm, $T_{ref} = 260$ K; w_{H_2O} is the molar fraction of water vapor; $C^0_{T_0,self}$, $C^0_{T_{ref},self}$ and $C^0_{T_0,frgn}$ are the reference spectral density function in Fig. B1 (a).

To get the mass absorption coefficients, a 'radiation field' R_f is applied [7,9],

$$R_f = \begin{cases} 0.5\nu\,\eta, & \text{for } \eta \leq 0.01 \\ \nu\,\frac{1-\exp(-\eta)}{1+\exp(-\eta)}, & \text{for } \eta \leq 10 \\ \nu, & \text{all other conditions} \end{cases} \quad \text{(B3)}$$

where η is a non-dimensional parameter defined as $\eta = \nu/(T/c_{r2})$ with $c_{r2} = 1.439$ cm K being the second radiation constant [9].

The continuum mass absorption coefficient for water vapor is then,

$$k^*_{cont,H_2O} = C(T,P)\,R_f. \quad \text{(B4)}$$

Fig. B1(b) plots the spectral and continuum absorption coefficients of pure water vapor, showing that continuum absorption dominates in the atmosphere window from 8 μm to 14 μm.
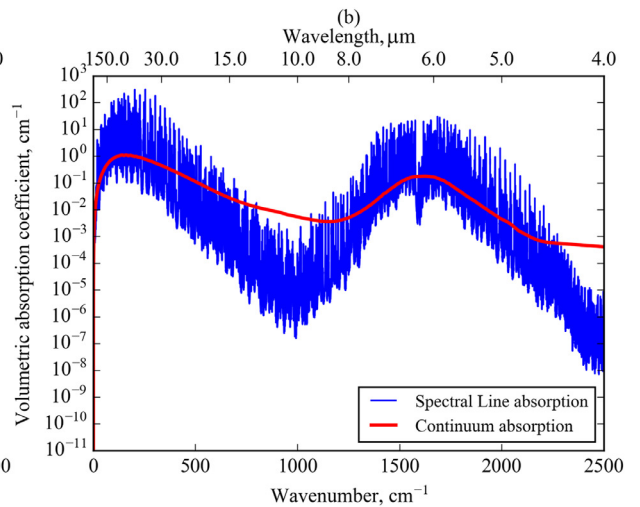
The continuum absorption spectral density functions C^0 at reference condition for CO_2 are obtained from the MT_CKD model [9] and plotted in Fig. B2 (a). For conditions with temperature T and pressure P, the spectral density function is,

$$C(T,P) = w_{CO_2}C^0_{T_{ref2}}f_c\frac{P}{P_0}\frac{T_0}{T}\left(\frac{T}{T_{ref2}}\right)^{f_t}, \quad \text{(B5)}$$

where $T_{ref2} = 246$ K; w_{CO_2} is the molar fraction of CO_2; $C^0_{T_{ref2}}$ is the reference spectral density function in Fig. B2 (a); f_c and f_t are the spectral and temperature correction factor obtained from [9], respectively. The continuum mass absorption coefficient for CO_2 is then,

$$k^*_{cont,CO_2} = C(T,P)\,R_f. \quad \text{(B6)}$$

Figure. B2 (b) plots the spectral and continuum absorption coefficients of pure CO_2, showing that continuum absorption dominates in the spectral from 6 μm to 8 μm.

Fig. B1. (a) The continuum absorption spectral density function C^0 for water vapor at selected conditions. (b) Spectral line and continuum absorption coefficients for water vapor at 1 atm and 288 K.
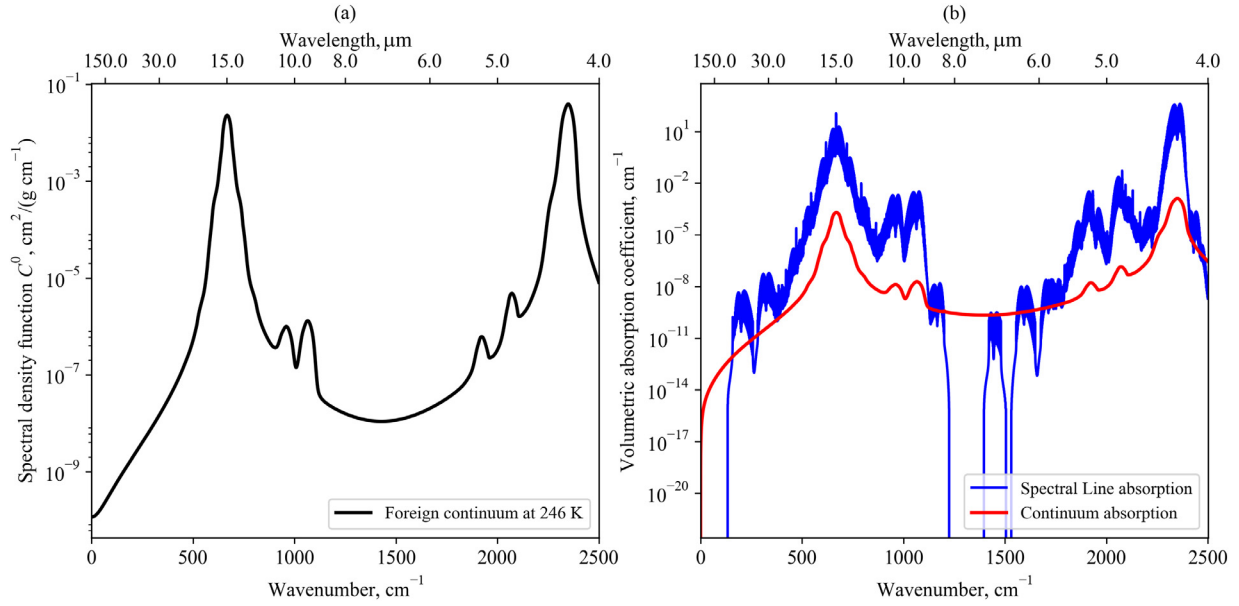
Fig. B2. (a) The continuum absorption spectral density function C^0 for CO_2 at selected condition. (b) Spectral line and continuum absorption coefficients for CO_2 at 1 atm and 288 K.

Appendix C. Derivation of transfer factors for the two-flux model

Consider the monochromatic attenuation of intensity along a path s,

$$\frac{dI}{ds} = \kappa_e(1 - \tilde{\rho})I_b + \kappa_e\tilde{\rho}\bar{I} - \kappa_e I, \tag{C1}$$

where the averaged intensity is the mean value over all solid angles, $\bar{I} = 1/4\pi \iint_0^{4\pi} I d^2\omega$.

For a plane parallel slab or atmosphere (Fig. C1), the irradiance G_n is expressed as,

$$G_n = \sum_j J_j \frac{1}{4\pi} \iint_0^{4\pi} \left[e^{t_s - t_{s,j}} - e^{t_s - t_{s,j+1}} \right] d^2\omega, \tag{C2}$$

where the optical depth $t_{s'} = \int_0^{s'} \kappa_e(s'')ds''$. Then the transfer factor between layer n and layer j is given by,

$$\mathcal{F}_{n,j} = \frac{1}{\Delta t_{s,n}} \int_{t_s} \int_0^{2\pi} d\phi \int_\theta \left[e^{t_s - t_{s,j}} - e^{t_s - t_{s,j+1}} \right] \frac{\sin\theta d\theta}{4\pi} dt_s. \tag{C3}$$

Let $u = 1/\cos\theta$, then $du = \sin\theta/\cos^2\theta d\theta$ and $\sin\theta d\theta = du/u^2$. Note that the transfer factors given above can be readily written in terms of the normal optical depth $t = \int_0^z \kappa_e(z')dz'$,

$$\mathcal{F}_{n,j} = \frac{1}{2\Delta t_n} \int_t \int_1^\infty \left[e^{(t-t_j)u} - e^{(t-t_{s,j+1})u} \right] \frac{du}{u^2}$$
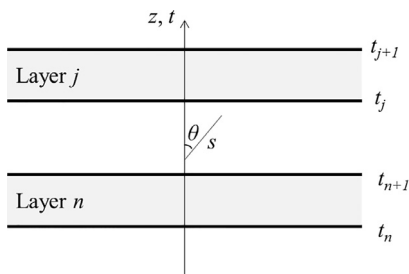
Fig. C1. Plane parallel geometry and layer indices.

$$= \frac{1}{2\Delta t_n} \int_{t_n}^{t_{n+1}} [E_2(t_j - t) - E_2(t_{j+1} - t)]dt$$

$$= \frac{1}{2\Delta t_n}[E_3(|t_j - t_{n+1}|) + E_3(|t_{j+1} - t_n|) - E_3(|t_j - t_n|) - E_3(|t_{j+1} - t_{n+1}|)]. \tag{C4}$$

The equivalent transfer area for a volume is defined as $A_n^* = 4\Delta t = 4\kappa_e\Delta z$, then the above Eq. (C4) yields Eq. (13).

Finally, for $j = n$,

$$\mathcal{F}_{n,n} = 1 - \frac{1}{2\Delta t_n} \int_{t_n}^{t_{n+1}} [E_2(t_n - t) - E_2(t_{n+1} - t)]dt$$

$$= 1 - \frac{1 - 2E_3(|t_{n+1} - t_n|)}{2(t_{n+1} - t_n)}. \tag{C5}$$

References

[1] Petty GW. A first course in atmospheric radiation. Madison, WI, United States: Sundog Pubulishing; 2006.
[2] Buehler SA, Von Engeln A, Brocard E, John VO, Kuhn T, Eriksson P. Recent developments in the line-by-line modeling of outgoing longwave radiation. J Quant Spectrosc Radiat Transfer 2006;98(3):446–57.
[3] Li M, Jiang Y, Coimbra CFM. On the determination of atmospheric longwave irradiance under all-sky conditions. Sol Energy 2017;144:40–8.
[4] Ridgway WL, Arking A. Computation of atmospheric cooling rates by exact and approximate methods. Journal of Geophysical Research: Atmospheres 1991;96(D5):8969–84.
[5] Clough SA, Shephard MW, Mlawer EJ, Delamere JS, Iacono MJ, Cady-Pereira K, et al. Atmospheric radiative transfer modeling: a summary of the AER codes. J Quant Spectrosc Radiat Transfer 2005;91(2):233–44.
[6] Buehler SA, Eriksson P, Kuhn T, Von Engeln A, Verdes C. ARTS- The atmospheric radiative transfer simulator. J Quant Spectrosc Radiat Transfer 2005;91(1):65–93.
[7] Berk A, Hawes F. Validation of MODTRAN® 6 and its line-by-line algorithm. J Quant Spectrosc Radiat Transfer 2017;203:542–56.
[8] Gordon IE, Rothman LS, Hill C, Kochanov RV, Tan Y, Bernath PF, et al. The HITRAN2016 molecular spectroscopic database. J Quant Spectrosc Radiat Transfer 2017;203:3–69.
[9] Mlawer EJ, Payne VH, Moncet J-L, Delamere JS, Alvarado MJ, Tobin DC. Development and recent evaluation of the MT_CKD model of continuum absorption. Philosophical Transactions of the Royal Society of London A: Mathematical, Physical and Engineering Sciences 2012;370:2520–56.
[10] Eddington A. On the radiative equilibrium of the stars. Mon Not R Astron Soc 1916;77:16–35.
[11] Sagan C, Pollack JB. Anisotropic nonconservative scattering and the clouds of Venus. J Geophys Res 1967;72(2):469–77.
[12] Brewster MQ, Tien CL. Examination of the two-flux model for radiative transfer in particular systems. Int J Heat Mass Transf 1982;25(12):1905–7.

[13] Toon OB, McKay C, Ackerman T, Santhanam K. Rapid calculation of radiative heating rates and photodissociation rates in inhomogeneous multiple scattering atmospheres. Journal of Geophysical Research: Atmospheres 1989;94(D13):16287–301.

[14] Edwards DK. The plating algorithm for radiation script-F transfer factor. J Heat Transfer 1986;108(1):237–8.

[15] Manabe S, Möller F. On the radiative equilibrium and heat balance of the atmosphere. Monthly Weather Review; 1961.

[16] Manabe S, Strickler RF. Thermal equilibrium of the atmosphere with a convective adjustment. J Atmos Sci 1964;21(4):361–85.

[17] Anderson GP, Clough SA, Kneizys FX, Chetwynd JH, Shettle EP. AFGL atmospheric constituent profiles (0.120 km). Tech. Rep.. DTIC Document; 1986.

[18] Alduchov OA, Eskridge RE. Improved Magnus form approximation of saturation vapor pressure. J Appl Meteorol 1996;35(4):601–9.

[19] Carbon Dioxide Information Analysis Center. Recent greenhouse gas concentrations. http://cdiac.ornl.gov/pns/current-ghg.html; 2016.

[20] Yu H, Chin M, Winker DM, Omar AH, Liu Z, Kittaka C, et al. Global view of aerosol vertical distributions from CALIPSO lidar measurements and GOCART simulations: regional and seasonal variations. Journal of Geophysical Research: Atmospheres 2010;115(D4).

[21] Lubin D, Satheesh S, McFarquar G, Heymsfield AJ. Longwave radiative forcing of Indian Ocean tropospheric aerosol. Journal of Geophysical Research: Atmospheres 2002;107(D19).

[22] Lesins G, Chylek P, Lohmann U. A study of internal and external mixing scenarios and its effect on aerosol optical properties and direct radiative forcing. Journal of Geophysical Research: Atmospheres 2002;107(D10).

[23] Yu H, Kaufman Y, Chin M, Feingold G, Remer L, Anderson T, et al. A review of measurement-based assessments of the aerosol direct radiative effect and forcing. Atmos Chem Phys 2006;6(3):613–66.

[24] Hale GM, Querry MR. Optical constants of water in the 200-nm to 200-μm wavelength region. Appl Opt 1973;12(3):555–63.

[25] National Oceanic and Atmospheric Administration. SURFRAD Network. http://www.esrl.noaa.gov/gmd/grad/surfrad/; 2015.

[26] Zhang J, Christopher SA. Longwave radiative forcing of Saharan dust aerosols estimated from MODIS, MISR, and CERES observations on terra. Geophys Res Lett 2003;30(23).

[27] Goody RM, Yung YL. Atmospheric radiation: theoretical basis, 1; 1989.

[28] Kochanov RV, Gordon IE, Rothman LS, Wcisło P, Hill C, Wilzewski JS. HITRAN Application programming interface (HAPI): a comprehensive approach to working with spectroscopic data. J Quant Spectrosc Radiat Transfer 2016;177:15–30.

[29] Edwards D.P.. GENLN2: A general line-by-line atmospheric transmittance and radiance model. version 3.0: Description and users guide1992;.

[30] Lee M. Scaling anisotropic scattering in radiation heat transfer for a planar medium. Urbana 1982;2:61801.

[31] Ellingson RG, Ellis J, Fels S. The intercomparison of radiation codes used in climate models: longwave results. Journal of Geophysical Research: Atmospheres 1991;96(D5):8929–53.

[32] U.S. Department of Energy. ICRCCM infrared (clear-sky) line-by line radiative fluxes (DB-1002). http://cdiac.ornl.gov/ndps/db1002.html; 2017.

[33] Liou KN. An introduction to atmospheric radiation, 84. Academic Press; 2002.

[34] Bohren CF, Huffman DR. Absorption and scattering of light by small particles. John Wiley & Sons; 2008.

[35] Mätzler C. MATLAB functions for Mie scattering and absorption, version 2. IAP Res Rep 2002;8:1–24.